Instrumentation for the Measurement of Sound Speed near the Ocean Surface

ERIC LAMARRE*

R. M. Parsons Laboratory, Department of Civil and Environmental Engineering, Massachusetts Institute of Technology, Cambridge, Massachusetts and Woods Hole Oceanographic Institution, Woods Hole, Massachusetts

W. K. MELVILLE

Scripps Institution of Oceanography, University of California, San Diego, LaJolla, California and R. M. Parsons Laboratory, Department of Civil and Environmental Engineering, Massachusetts Institute of Technology, Cambridge, Massachusetts

ABSTRACT

Air bubbles entrained by breaking waves in the ocean surface layer can dramatically alter the velocity and attenuation of acoustic waves. The development of an effective technique for directly measuring the sound speed near the ocean surface is reported. The method makes use of the travel time of short acoustic pulses between a transmitter and a receiver separated by 40 cm. Phase distortions caused by acoustic reflections from the surface or from nearby buoy structural elements are separated in time from the direct path signal. A DSP-based data processing system was implemented to cross correlate the transmitted and received acoustic pulses and thus yield sound-speed measurements in real time. Perhaps the most significant novelty of the present measurement technique is its ability to make simultaneous measurements of the sound speed at several depths, starting as close as 0.5 m to the surface, at frequencies down to 5 kHz, and at a sample rate of 4 Hz per channel. Furthermore, the technique is direct and thus avoids the many difficulties involved with inferring the sound speed from in situ bubble population measurements. Results from controlled tests in the laboratory and in a lake are presented. The results confirm the validity of the technique and establish basic performance criteria. Data from the field that demonstrate the operation of the instrument in an ocean environment are also presented.

1. Introduction

Air bubbles are entrained in the water column by the breaking of surface waves. Although bubbles have been observed down to a depth of the order of 10 m, usually they are located within 1 or 2 m of the ocean surface (Thorpe 1982; Farmer and Vagle 1989; Zedel and Farmer 1991). Air bubbles have been found to form distinct plumes and clouds that are the result of breaking waves and subsequent advection by Langmuir circulations (Thorpe 1982; Farmer and Vagle 1989; Lamarre and Melville 1992). These bubble plumes and clouds are believed to be responsible for the high levels of acoustic reverberation observed at the ocean surface at wind speeds in excess of 10 m s^{-1} (Henyey 1991). Air bubbles also have an important role in fluxes through the ocean surface layer because of their ability to increase the effective transfer rate of heat and gases between the atmosphere and the ocean (Thorpe 1982;

Merlivat and Memery 1983; Woolf and Thorpe 1991; Wallace and Wirick 1992).

In the presence of bubbles, the velocity of sound in water can be significantly altered. At frequencies below bubble resonance, the sound velocity is strongly dependent on the total volume fraction of air in the water (hereafter void fraction). In fact, void fraction and sound speed at frequencies much less than bubble resonances are related through Wood's equation (refer to appendix A for details) with void fractions in the range 10^{-6}–10^{-2} corresponding to sound-speed reduction in the range 100–1400 m s^{-1}, respectively. These sound-speed reductions are very large compared to fluctuations caused by changes in temperature, salinity, or density that typically range from a few to tens of meters per seconds and vary on comparatively longer timescales of the order hours and longer. Thus, Wood's equation permits one to calculate the concentrations of air near the ocean surface by simply measuring the low-frequency sound speed.

Sound is a powerful tool that can be used to remotely monitor upper-ocean processes. For example, passive techniques include the monitoring of wind speeds (Vagle et al. 1990) and rainfall rates (Nystuen 1986; Laville et al. 1991) over the oceans and the detection of breaking waves (Ding 1992). It is also hoped that

---

* Current affiliation: Collège des Ingénieurs, Paris, France.

Corresponding author address: Dr. W. K. Melville, Scripps Institution of Oceanography, University of California, San Diego, La Jolla, CA 92093-0213.

JOURNAL OF ATMOSPHERIC AND OCEANIC TECHNOLOGY VOLUME 12

in the near future we may be able to remotely sense the dissipation of surface wave energy by breaking (Loewen and Melville 1991) and the transfer rates of gases across the air–sea interface (Lamarre and Melville 1991). However, many of the benefits offered by acoustic remote sensing near the ocean surface depend on a prior knowledge of the propagation characteristics between the source (i.e., the phenomenon being observed) and the receiver located at some depth below the surface (Buckingham 1991). Without this information, it is difficult to separate acoustic features that are caused by the source from those caused by the medium through which the sound must propagate. Since the rough water surface and the air bubbles below it dominate the nature of sound propagation near the surface, it is imperative that we have a good description of the spatial and temporal changes in the sound speed and attenuation field within that bubbly region.

The motivation for measuring the speed of sound near the ocean surface is therefore twofold. First, the concentrations of air in the ocean surface layer can be calculated from measurements of the low-frequency sound speed. Clearly, this would yield useful data for the study of air–sea gas transfer. Second, acoustic remote sensing techniques and surface reverberation models require the knowledge of sound propagation characteristics near the ocean surface.

Only a few previous studies have been conducted on the measurement of sound speed near the ocean surface. Medwin and his coauthors (Medwin 1974, Medwin et al. 1975) made measurements of sound-speed fluctuations near the surface with a CW signal transmitted between two horizontal hydrophones at various frequencies in the range 15–100 kHz. The sound speed was computed by measuring phase shifts at sea and by comparing them to a reference phase shift in bubble-free water. Their instrument had a high resolution (0.1 m s^{-1}) but it was limited to a minimum measurement depth of 3 m in order to minimize surface reflections that would have corrupted the phase. Their results showed maximum sound-speed anomalies in the range 10–15 m s^{-1} at depths greater than 3 m during light wind conditions. This suggests that higher values are likely to be found closer to the surface and in higher sea states.

Farmer and Vagle (1989) used a multifrequency upward-looking sonar to measure the bubble density at four discrete bubble sizes at depths ranging from 0.1 to 10 m. From these measurements, they inferred the shape of the bubble population. They computed the time-averaged sound-speed profiles by integrating the dispersive effects of all bubbles using a well-known integral equation that takes as input the bubble population (Clay and Medwin 1977, appendix 6). Their data showed that sound-speed anomalies are the largest at the surface (3–15 m s^{-1}) for wind speeds between 10 and 12 m s^{-1} and decrease exponentially with depth with an e-folding depth of approximately 1.4 m.

Bubble size distributions in the upper ocean are usually described by power laws. The integral equation for the sound speed can be very sensitive to the exact value of the exponents of these power laws and the upper and lower bubble size limits on the integral itself. For example, Farmer and Vagle (1989) determined from their measurements of bubble densities at 16, 37, 65, and 116 μm that the peak of the population was located between 16 and 37 μm with a probable location near 20 μm but the exact position could not be established. For bubbles larger than the peak size, they found slopes between a^{-4} and a^{-6}, which is consistent with the literature for bubbles up to 60 μm but is not consistent for larger bubbles that have been found by many investigators to have an $a^{-2.5}$ to $a^{-3.0}$ slope (Medwin 1970, 1977; Baldy 1988; Medwin and Breitz 1989; Su et al. 1993).

We can appreciate the effect of a different slope above, say, 60 μm by computing the low-frequency sound speed with a bubble population having the same characteristics as described above but with an a^{-4} slope in one case and an $a^{-2.5}$ slope in the other for bubbles greater than 60 μm. The number density of bubbles at the peak of the population near the surface is obtained from Farmer and Vagle's paper (1989) and the computation is carried from 1 μm up to a maximum bubble radius of 400 μm. The sound-speed reduction with an a^{-4} slope is found to be 26.8 m s^{-1}, which is comparable to Farmer and Vagle's (1989) computations at the surface for their lowest frequency and highest wind speed, and the reduction with an $a^{-2.5}$ slope is 97.2 m s^{-1}, a factor of 3.6 greater. A similar calculation with the peak of the population varying between 16 and 24 μm shows that the sound-speed reduction would vary by a factor of 2. Variations in the upper limit of the integral can generate even greater discrepancies, especially when the slope of the population is small (say, $a^{-2.5}$ to $a^{-3.5}$). Thus, it is clear that sound-speed calculations based on integration of bubble population data are very sensitive to the exact shape of the bubble population and the location of its upper and lower limits for which there are still large discrepancies in the literature.

Other limitations of upward-looking sonars include the difficulty of differentiating surface scattering from scattering by the dense bubble layer immediately below the surface that will affect the exact determination of the surface. The large spot size of the sonar, especially at low frequencies, will also make it difficult to differentiate between the crest and the trough of the shorter waves (e.g., a 28-kHz sonar with an 18° beamwidth and located at 30 m will have a spot size of 9.4 m). Other complexities include the issue of multiple scattering, which is not taken into account with the sonar technique and which may become significant near the surface where the bubble density is important.

Measurements of sound speed by Medwin and his co-authors were limited to a minimum depth of 3 m

and a minimum frequency of 15 kHz. Farmer and Vagle's measurements had the distinct advantage of being nonintrusive, but they were impeded by the difficulties in computing the sound velocity from bubble population data and by the limitations of echo sounders very close to the ocean surface where the void fractions can be high. Furthermore, the above studies have focused on a time-averaged (approximately 10 min) description of the sound speed and do not describe the short-term fluctuations. In this paper, an instrument using a direct technique capable of measuring the speed of sound at six different depths is reported, with the shallowest one being 0.5 m, at a rate of four measurements per second, and over a frequency range of 5–40 kHz. The instrumentation and the methodology is described in detail and laboratory and lake tests are presented that validate the technique. Some field data are also presented that show the operation of the instrument in an ocean environment. Appendix A gives a brief exposition on Wood's equation and appendix B addresses the issue of group velocity versus phase velocity.

2. Instrumentation

A light buoy was built to carry the probes and instrumentation (Fig. 1a). The buoy was equipped with six acoustic sound-speed measuring modules. Each module included a transmit and a receive omnidirectional hydrophone both rigidly supported on a stainless steel rod (Fig. 1b). The omnidirectional transmit hydrophone was an ITC-1042 (International Transducer Corporation, Santa Barbara, CA) and the omnidirectional receive hydrophone was an ITC-1089E. The characteristics of their horizontal beam pattern are ±0.5 dB up to 80 kHz and ±1.0 dB up to 40 kHz, respectively.

Our choice of using separate transmit and receive hydrophones instead of a single transmit–receive hydrophone with a reflecting plate was guided by the experiments of Medwin (1977). He concluded that the latter configuration was inadequate for accurately measuring sound speed because of phase shift problems occurring at the reflector.

Other instrumentation on the buoy included a Sea-Bird SBE 3 temperature sensor that was used to calculate the speed of sound in bubble-free water. An NEC TI-23A video camera mounted inside a Video Vault (Spring, Texas) underwater housing was used to image the bubble plumes and clouds formed at or near the buoy. From the video measurements, it was found that the buoy tracked the water surface to within ±10 cm in winds up to 10 m s^{-1} and wave heights of the order of 1 m. An 88-kHz Furuno model FCV-561 upward-looking sonar was mounted at the bottom of the buoy. The sonar was used to image the bubble clouds as has been previously done by Thorpe (1982) and Farmer and Vagle (1989), among others. These sonar results are reported elsewhere (Lamarre and Melville 1994).
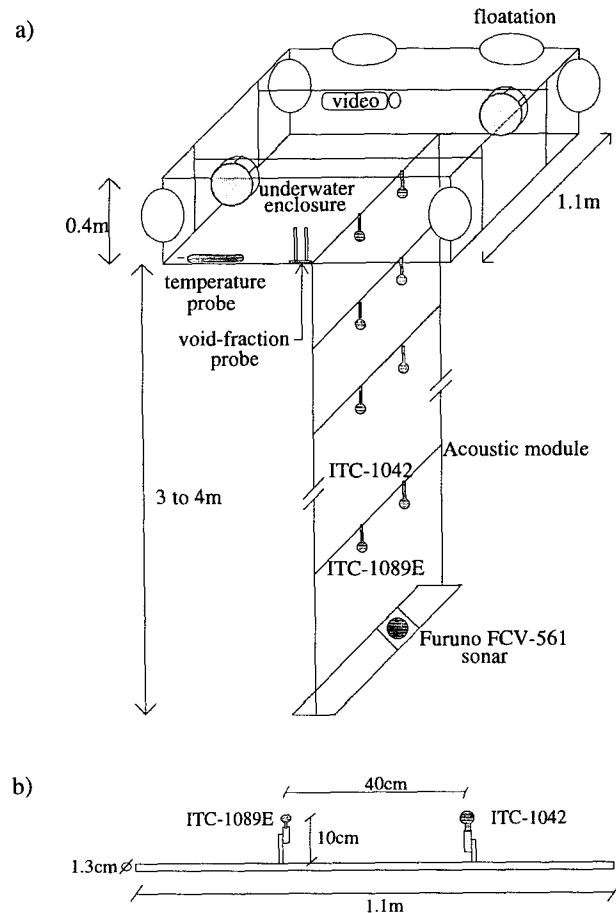

FIG. 1. (a) Sketch of the buoy and its instrumentation. (b) Sketch of the hydrophone support module.

Two 150-m underwater multiconductor cables served as links between the buoy and the instrumentation on board the ship. The cables were connected to two underwater enclosures mounted on the buoy. The enclosures served as junction boxes between the buoy probes and the multiconductor cables. The buoy was tethered from a ship that was maneuvered to keep the buoy abeam and free of the wind and wave wake of the ship as much as possible and to keep the tether slack at all times.

The support module that holds the transmit and receive hydrophones is shown in Fig. 1b. The bodies of the hydrophones are held by thin sleeves that are welded to 6-mm-diameter vertical rods that in turn are welded to the main supporting rod 13 mm in diameter. All members are made of stainless steel with minimal member cross-sectional dimensions and thus minimal acoustic reflections. Extensive transmit–receive tests at various frequencies were performed in a large water tank with and without the stainless steel support module. They showed that the presence of the support module did not alter the shape or the amplitude of the received pulse in the frequency range from 5 to 40

kHz. The support rod is attached on both sides to the buoy's main vertical members. The reflective path to these vertical members is made long enough to delay the acoustic reflections from contaminating the direct path signal.

3. Balancing acoustic frequency, pulse length, separation of hydrophones, and depth of measurements

The sound-speed measurement technique is based on estimating the travel time of an acoustic pulse as it propagates from a transmitter to a receiver. The time delay is computed by cross correlating the transmit and received pulses and by locating the peak in the cross-correlation function. Since the distance between the hydrophones is constant, one can readily compute the speed of sound in the bubbly mixture from the knowledge of the time delay. It is critical, with this technique, to eliminate or at least minimize any reflections of the acoustic pulse by nearby objects or by the water surface that would bias the location of the peak in the cross-correlation function.

The elimination of unwanted reflections was realized by separating in time the direct path signal from the reflected signal. This requires balancing four parameters: 1) the acoustic pulse frequency f (or more precisely the wavelength $\lambda = Cf$, where C is the speed of sound in water or in the bubbly mixture), 2) the pulse length L_p, 3) the separation distance between the transmit and receive hydrophone L_d (i.e., the direct path), and 4) the depth of the hydrophones. The depth of the hydrophones is important because in our application the reflection from the surface is the dominant and often the closest reflective path. Note that the pulse length $L_p = N\lambda$, where N is the number of periods. Balancing these parameters requires that

$$L_p + L_d < L_r \qquad (1)$$

where L_r is the length of the closest reflective path. In essence, this equation states that reflections from nearby objects or from the water surface must arrive at the receiving hydrophone after the entire pulse from the direct path has reached the receiver. The determination of each of the above three lengths requires careful compromises that will greatly influence the characteristics and performance of the instrument.

Due to their limited bandwidth, underwater transducers are restricted in their ability to transmit short sound pulses. For the spherical transducers used in our experiments, two to three periods is about the minimum that can be achieved. This therefore sets a lower bound on N ($N = 2$–3). The lowest usable frequency is dictated by the proximity of the surface and by the ability of the transducer to transmit sound with high enough acoustic intensity to dominate the ambient noise. For a small 2–3-cm-diameter spherical transducer, this lower limit is approximately 3–6 kHz. Lower

frequencies can be achieved with larger transducers, but their size makes them difficult to deploy and they are significantly costlier.

One of the novelties of this study was the direct measurement of sound speed close to the surface. Assuming that the transmit and receive hydrophones are positioned at the same depth d (i.e., the pulse propagates horizontally), the length of the reflective path from the surface is given by

$$L_r = 2\left[d^2 + \left(\frac{L_d}{2}\right)^2 \right]^{1/2}. \qquad (2)$$

Using Eqs. (1) and (2) and assuming $L_p \approx 2.0\lambda$ we can construct a table of L_d as a function of hydrophone depth d and acoustic frequency f (see Table 1).

The length of the direct path L_d must be kept short enough to permit measurements as close to the surface as possible and long enough to obtain a meaningful spatial average. We selected a direct path of length $L_d = 40$ cm and a minimum transmit acoustic frequency of 5 kHz. Of course, any frequency above 5 kHz can also be used. The number of periods in the pulse was set at 2–3, the minimum achievable. Table 1 gives $d = 0.5$ m as being the smallest achievable depth with the parameters selected.

The transmit and receive acoustic systems are shown in Fig. 2. The boxes with a double line around them refer to expansion cards mounted inside a PC ALR-Veisa 386-33-MHz computer. The computer was equipped with an expansion chassis from Industrial Computer Source model NODE/XTC/ATC-D to accommodate the large number of expansion cards (a total of seven). The transmit and receive systems are synchronized by a pulse generator that acts as the main control clock. The pulse generator triggers the signal generator that in turn transmits the waveform recorded in its RAM to a power amplifier. The amplitude of the signal transmitted by the signal generator was computer controlled. After the power amplifier stage, the pulse is routed to the appropriate transmit hydrophone by a bank of high-power mechanical relays that are controlled by a digital I/O card. The signal travels from the ship to the transmit underwater enclosure located on the buoy through an underwater cable made of individually shielded paired conductors. The underwater

TABLE 1. Maximum length of the direct path L_d (m) as a function of acoustic frequency f and hydrophone depth d. The transmit and receive hydrophones are assumed to be at the same depth. The length of the acoustic pulse $L_p = 2\lambda$, where λ is the acoustic wavelength.

	d (m)			
f	0.25	0.5	0.75	1.0
2.5 kHz ($\lambda = 0.6$ m)	—	—	0.3	1.05
5.6 kHz ($\lambda = 0.3$ m)	—	0.55	1.55	3.0
10.0 kHz ($\lambda = 0.15$ m)	0.25	1.5	3.6	6.5

a)

```
┌─────────────────────────┐
│   pulse generator       │ ──→ to D/A
│  Signametrics SM-1005   │     board
└─────────────────────────┘
            │
            ↓
┌─────────────────────────┐
│   signal generator      │ ──→ to receive
│  Signametrics SM-1020   │     high-pass filter
└─────────────────────────┘
            │
            ↓
┌─────────────────────────┐
│    power amplifier      │
│    Ramsa WP-9110        │
└─────────────────────────┘
            │
            ↓
┌────────────────────────────────┐    ┌──────────────────────────┐
│ 6 high-power mechanical relays │ ←──│  24 bits digital i/o card │
│      Metrabyte SRA-01          │    │    Metrabyte PIO-12       │
└────────────────────────────────┘    └──────────────────────────┘
            │
          6 │   underwater cable
            │   Simcona - 130m
            ↓
┌────────────────────────────────┐
│  transmit underwater enclosure │
└────────────────────────────────┘
    ○   ○   ○   ○   ○   ○

      6 hydrophones - ITC-1042
```

b)

```
            6 hydrophones - ITC-1089E
    ○   ○   ○   ○   ○   ○
┌────────────────────────────────┐
│  receive underwater enclosure  │
│   6 pre-amplifiers - 40dB      │
│        Ithaco 144F             │
└────────────────────────────────┘
            │
          6 │  underwater cable - coax
            │  Simcona - 130m
            ↓
transmit    ┌────────────────────────────────┐
signal  ──→ │  7 digitally programmable      │ ←──
            │     high-pass filters          │
            │   Frequency Device 874         │
            └────────────────────────────────┘
                         │ 6
                         ↓
            ┌────────────────────┐    ┌──────────────────────────┐
            │   6 Amplifiers     │    │  24 bits digital i/o card │
            │   Wilcoxon AM-5    │    │    Metrabyte PIO-24       │
            └────────────────────┘    └──────────────────────────┘
                         │ 6
                         ↓
            ┌────────────────────────────────┐
            │  7 digitally programmable      │ ←──
            │     low-pass filters           │
            │   Frequency Device 844         │
            └────────────────────────────────┘
                         │ 7
                         ↓
            ┌────────────────────────────────┐
            │   data acquisition board       │ ←──── pulse generator
            │   RC Electronics ISC-16E       │         signal
            └────────────────────────────────┘
                    ↑          ↓
    ┌──────────────────────┐  ┌──────────────────────┐
    │   DSP board          │  │   SCSI adapter       │
    │ Spectrum TMS320C30   │  │ Future Domain TMC-1660 │
    └──────────────────────┘  └──────────────────────┘
                                       ↓
                              ┌──────────────────────┐
                              │   optical storage    │
                              │ Pinnacle Micro PMO-650 │
                              └──────────────────────┘
```
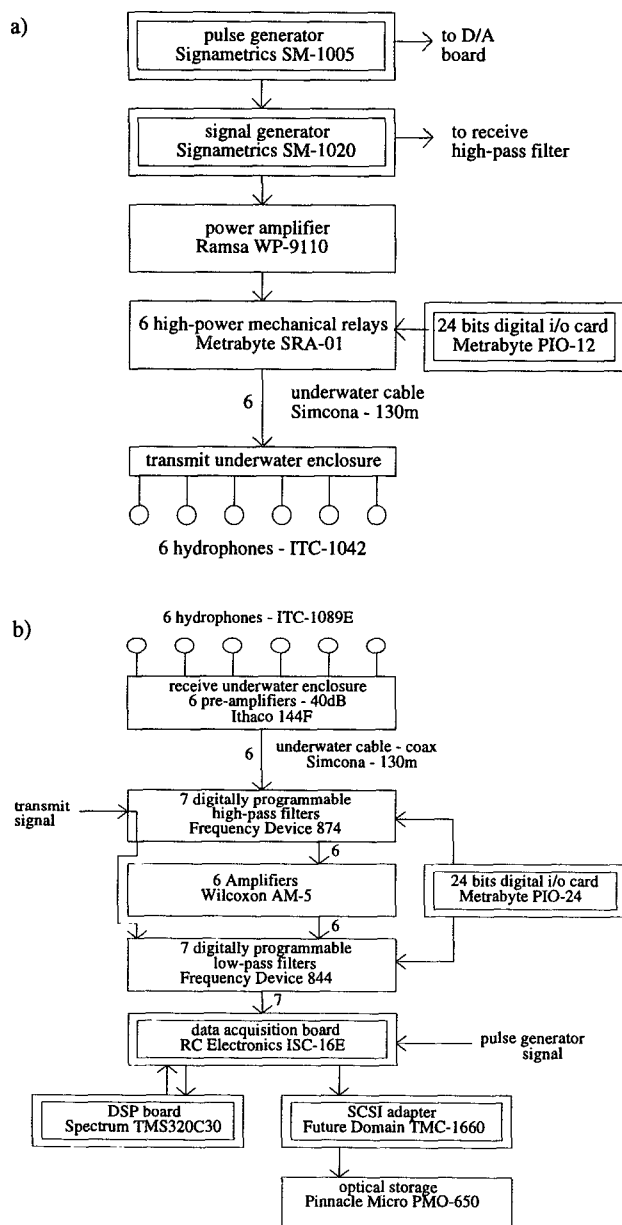
FIG. 2. Block diagram of (a) transmit acoustic system
and (b) receive acoustic system.

enclosure acts as a junction box between the six trans-mitters and the long underwater cable.

The transmitted pulse is received by a hydrophone located at a horizontal distance of 40 cm horizontally away from the transmit hydrophone (see Fig. 1b). The received signal is first amplified by a 40-dB preamplifier located in the receive underwater enclosure on the buoy. After this amplification stage, the signal is carried back to the ship via an underwater cable made of RG-174 coaxial cables. The use of separate enclosures and cables for carrying the signals to and from the ship was

necessary in order to reduce electrical cross talk of the transmit pulse on the receive signal.

At the ship, the receive acoustic pulse is passed through a high-pass filter, a second 40-dB amplification stage, and a low-pass filter. The cutoff frequencies of the filters were digitally programmable from the computer with the help of a digital I/O card. Notice that the transmit pulse is also passed through the filter bank in order to match the inherent time delays introduced by filtering. Finally, the conditioned signals were sampled by a 1-MHz data acquisition board. Real-time processing of the transmit and received pulses was performed by a dedicated DSP board and the results along with the raw data were stored on 600-Mbyte optical disks. The details of the data acquisition and data processing technique are explained in subsequent sections.

Figure 3a shows typical field data of transmit (above) and receive (below) acoustic pulses at 10 kHz. The transmit and receive hydrophones were both located at a depth of 0.5 m. The direct acoustic path and the reflection from the surface are clearly visible. Figure 3b shows the spectra for the time series shown in Fig. 3a. The second lower line on the receive spectra of Fig. 3b represents measured ambient noise level for wind speeds around 8 m s^{-1} (including ship noise). The pulses are therefore 30–40 dB above the ambient noise level, which would give a signal-to-noise ratio of 50–100.

4. Real-time data acquisition and data processing

In this section and the next, we describe in detail the real-time data acquisition and data processing systems. The ability to do real-time monitoring of the sound-speed fluctuations was a very valuable feature, especially during the field experiments. Problems could
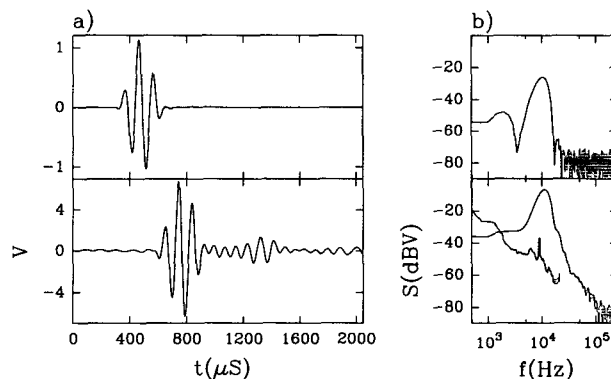

FIG. 3. (a) Time series of transmit (above) and receive (below) 10-kHz acoustic pulses. (b) Spectrum of time series in (a). Note that the receive time series was windowed with a 250-point Bartlett window in order to eliminate the reflections from contributing to the spectrum. The second line on the lower spectrum is the ambient sound for W_s = 8 m s^{-1} including ship noise. The small spike in the lower spectrum at approximately 10 kHz is due to electrical noise. Data from a field experiment in Buzzards Bay, Massachusetts.

be detected immediately and various alternatives for the sampling rate and the depth of the hydrophones could be investigated.

a. Data acquisition and computation of the time delay

The data acquisition system is made up of three major block components as shown in Table 2. The primary block deals with initialization of various boards. First, the frequency of the pulse generator is set (refer to Fig. 2a). The signal generator, which transmits the acoustic pulse, is then enabled. Next, the cross-correlation code is uploaded to the DSP board and the program is reset and put on standby. Finally, the real-time graphic windows are initialized and also put on standby.

The second block constitutes the core of the system. All instructions in the block must be performed in order to complete one measurement of the sound speed at a specific depth. First, one of the six transmit hydrophones is selected by a 24-bit digital I/O card that enables a bank of high-power mechanical relays (refer to Fig. 2a). Next, the 12-bit data acquisition board is initialized for the proper sample rate, channel selection, and trigger mode. The channel selection defines which receiving hydrophone is selected. The selected transmit and receive hydrophones are always located on the same support module. The data acquisition is then placed on hold as it waits for the trigger from the pulse generator. After reception of the trigger, the transmit and receive pulses are sampled at 500 kHz each for a duration of 2048 μs. This sample window is long enough to accommodate sound-speed anomalies as large as 1200 m s^{-1}. After sampling is completed, the two 1024 data arrays are downloaded from the data acquisition board and stored on a 4-Mbyte RAM disk. The RAM disk was used as a temporary fast storage device before the final transfer to optical disk.

The transmit and receive data arrays are then uploaded to the DSP board for computation of the cross correlation using the fast Fourier transform (FFT) method. The forward FFTs of the two arrays to be cross correlated are computed first. The resulting complex arrays are multiplied to obtain the cross-spectrum, which is finally run through an inverse FFT to obtain the real cross-correlation array. The location of the peak in the cross-correlation array immediately gives the time delay. The DSP board gave a factor-of-5 improvement over the PC performance for cross-correlation computations. This included all the overhead time required to pass the data from the PC to the DSP board. Furthermore, the ability of the DSP board to run in parallel with the PC processor gave a further factor of 2 increase in performance. Upon completion, the computed time delay (and thus sound speed) is downloaded back to the PC where it is displayed by a real-time graphics routine. The operations of the second

TABLE 2. The three block components of the data acquisition system

Initialization
- Initialization of transmit system
- Initialization of DSP board
- Initialization of real-time graphics

Real-time data acquisiton and data processing loop
- Selection of transmit hydrophone
- Initialization of data acquisition board
- Selection of receive hydrophone
- Data acquisition board waits for trigger
- After reception of trigger, sampling proceeds
- Data are written to RAM
- Data are uploaded to DSP board
- Computation of time delay on DSP board
- Cross-correlation result downloaded from DSP
- Result displayed on screen

Data acquisition of support sensor and data storage
- Sampling of temperature probe
- Read video time-code generator
- Transfer data from RAM to optical disk
- Write cross-correlation results to optical disk

block are repeated for each new sound-speed measurement. The peak performance of the system permitted sampling of all six transmit–receive modules at 4 Hz. This gave a total of 24 sound-speed measurements per second. At that rate, it took 40 s to fill the 4-Mbyte RAM disk with raw data. At sea, the system was modified to save only the raw data on every other sound-speed measurements. Hence, data were taken continuously for 80 s before the buffer was full.

The third and final block in Table 2 samples the water temperature and reads the video time-code generator. Finally, the computed time delays and the data stored to RAM (nearly 4 Mbyte) are transferred to optical disk. The Pinnacle Micro PMO-650 optical drive accomplished this task in 10 s.

b. Interpolation of the cross correlation

A sampling rate of 500 kHz per channel gives a 2-μs resolution on the location of the peak of the cross correlation. Considering that the location of the peak will be around 267 μs (i.e., 0.4-m path divided by 1500 m s^{-1}), this gives a resolution of 0.7% (or 10 m s^{-1}) on the determination of the speed of sound. We can further increase this resolution by making use of the very high signal-to-noise ratio of the receive pulse (SNR $\approx 10^2$) and its narrow bandwidth. These two properties of the transmit and receive signal give a very smooth cross-correlation function that can be interpolated to increase the resolution of the exact position of the cross-correlation peak.

Nine sampled data points located around the peak of the cross-correlation function are used in a cubic-spline routine to compute the interpolation. The interpolation is performed on a grid 20 times finer than the original. The computation of the interpolation is
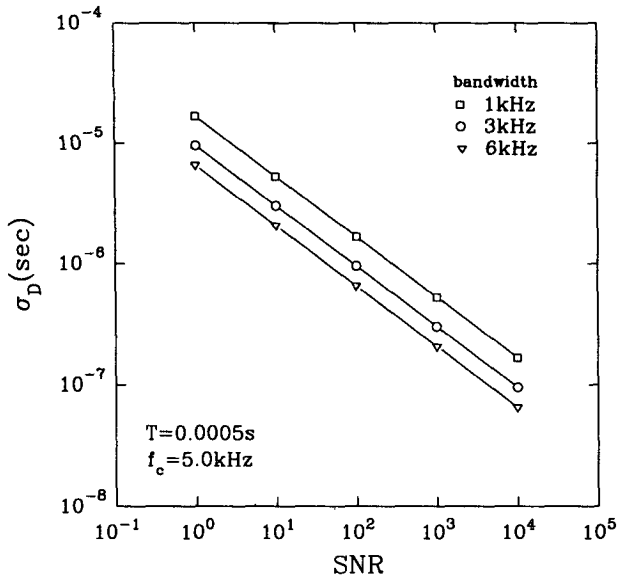
FIG. 4. Cramer–Rao lower bound on the standard deviation of the time-delay estimate σ_D for an observation time $T = 0.0005$ s, a signal frequency $f_c = (f_1 + f_2)/2 = 5$ kHz, and a signal bandwidth $f_2 - f_1 = 3$ kHz. Note that results are also shown for 1- and 6-kHz bandwidths. For the laboratory, SNR $\sim$ 1000 and in the field SNR $\sim$ 100.

very fast and it adds a negligible amount to the computation time of the cross-correlation. The laboratory tests, discussed subsequently, show that this interpolation technique can give an $O(10)$ increase in the resolution of the sound-speed measurements in laboratory conditions.

c. Cramer–Rao lower bound on the standard deviation of the time-delay estimate

The Cramer–Rao lower bound is a well-known relationship in active and passive target localization systems (for a review, see Quazi 1981). The relationship gives a lower bound on the standard deviation of the time-delay estimate given that the observation time T, signal-to-noise ratio SNR, and signal bandwidth f_2-f_1 are known

$$\sigma_D \geqslant \left(\frac{3}{8\pi^2 T}\right)^{1/2} \frac{1}{(\text{SNR})^{1/2}} \frac{1}{(f_2^3 - f_1^3)^{1/2}}. \quad (3)$$

In essence, the Cramer–Rao lower bound states that for known signal characteristics the minimum standard deviation on the time-delay estimates will be given by Eq. (3). For example, Fig. 4 shows how σ_D varies as a function of SNR for an observation time T and a bandwidth f_2-f_1 consistent with the 5-kHz pulses used in the present study for measuring the speed of sound. The SNR in the field was shown to be approximately 100 (Fig. 3), while in the laboratory we have obtained an SNR closer to 1000. Figure 4 predicts that mea-

surements of the time delay conducted in the laboratory will have a standard deviation of approximately 0.3 μs at best, while field estimates of the time delay will be closer to 1.0 μs. Of course, this is for a single estimate of the time delay. Statistical averaging would further decrease these standard deviations. The next sections on the laboratory tests and field measurements of the sound speed will show that these lower-bound estimates of σ_D were close to what was actually achieved with the acoustic system.

5. Laboratory and lake tests

a. Changes in time delay caused by changes in the distance between the transmitter and the receiver

A controlled test of the acoustic instrument was performed by varying the distance between the transmit and receive hydrophone. For this test, the acoustic module was modified by cutting it in half along its center line (Fig. 5a). The two halves were slid in a locking sleeve that permitted increasing or decreasing the separation distance between the hydrophones. The separation distance was varied between 400 and 425 mm. Small screws were installed on each half to act as reference marks for an exact measurement of the change in separation Δs_a given with respect to an initial separation of 400 mm. The measurements Δs_a were obtained with a micrometer accurate to 0.03 mm. With the acoustic system, the measured change in separation Δs_{td} was obtained by multiplying the change in time delay by the sound speed computed from temperature measurements (Del Grosso 1974; Medwin 1975).
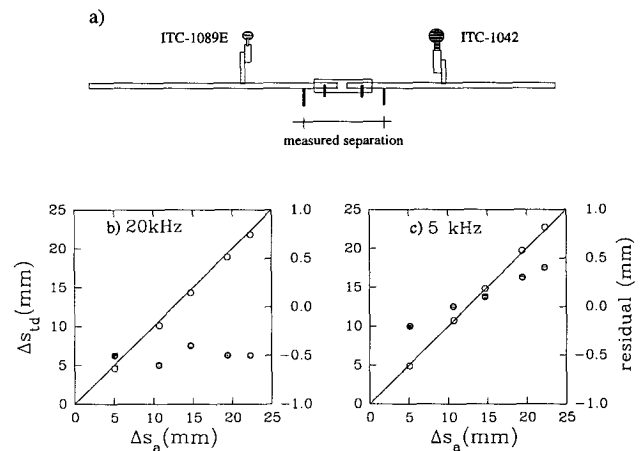

FIG. 5. (a) Modified support for varying the distance between the transmit and receive hydrophone. (b) and (c) Changes in transmitter–receiver separation. The separation distance was varied between 400 and 425 mm. Only the change in separation Δs with respect to the 400-mm reference is plotted; Δs_a measured with a micrometer; Δs_{td} measured from changes in time delays. (b) 20 kHz. (c) 5 kHz. Actual measurements (O) and residual (●). Note that the vertical scale for the residual is on the right hand side of the graphs.
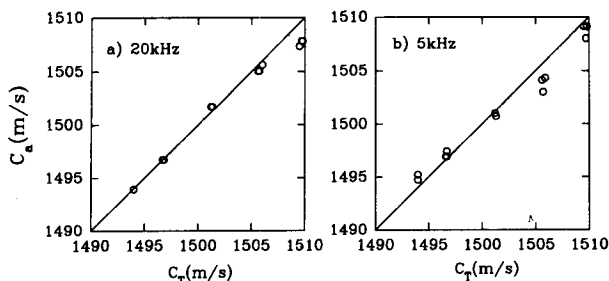
FIG. 6. Changes in sound-speed caused by changes in temperature. C_T from temperature measurements and C_a from sound-speed measurements. (a) 20 kHz. (b) 5 kHz.

Results for 20- and 5-kHz pulses are presented in Figs. 5b and 5c. Notice that the solid symbols have their vertical axis on the right-hand side and they represent the residual $\Delta s_a - \Delta s_{td}$. These results give solid support to the acoustic technique and show that in ideal laboratory conditions, the typical errors over a 40-cm path are within ±0.5 mm or ±0.13%. Accordingly, this suggests that sound-speed measurements made over a fixed distance of 400 mm will have a typical resolution of ±0.13% (±2 m s^{-1}). This error is likely to increase at sea because of higher ambient noise levels, fluid velocity, and buoy motion.

b. Changes in sound speed due to changes in water temperature

A test was performed in a laboratory tank by varying the water temperature by introducing warm or cold tap water. The temperature was measured with a Sea-Bird SBE 3 probe and the sound speed calculated using a standard equation (Del Grosso 1974; Medwin 1975). After bringing the water to a new temperature, the tank rested for 3–4 h to allow the fresh tap water to degas and for the temperature in the tank to become uniform. Each measurement consisted of an average of five sound-speed measurements separated by 1 s.

The results for two frequencies are shown in Fig. 6. The horizontal axis is the sound speed calculated from temperature measurements. The vertical axis is the actual measurement of sound speed. Overall the results are very good. Clearly, the sound-speed measuring system has the ability to detect small changes in the speed of sound even at frequencies as low as 5 kHz. The small deviations observed at higher sound speeds may have been caused by poor water quality or incomplete degassing of the water at higher temperature.

c. Lake test

A trial experiment was conducted in the Mystic Lake (Medford, Massachusetts) in early September 1992. At that time of the year, New England lakes still have their summer temperature stratification. Typical temperature differences between the surface and 10 m be-

low can range from 10° to 20°C. This corresponds to sound-speed differences of 30–50 m s^{-1}. This was therefore an ideal setting for testing the entire system with a large and stable sound-speed gradient. The buoy was positioned in water 20-m deep and approximately 100 m away from shore. The buoy was stripped of its flotation and gradually lowered in the water column by steps of 0.5 m. Five acoustic modules measured the sound speed at different depths and measurements from a temperature probe were used to calculate the temperature-dependent sound-speed profile.

Results of the experiment are shown in Fig. 7 for two different acoustic frequencies. The solid line is a spline fit through the sound-speed data calculated from temperature measurements. The results show very good tracking of the sound-speed profile by the acoustic technique. The 20-kHz data show less scatter because of the higher SNR at that frequency.

6. Field measurements

Two ocean experiments have been conducted on the measurement of sound speed and attenuation near the ocean surface with the instrumentation described in this paper. The results from these experiments are reported elsewhere (Lamarre 1993; Lamarre and Melville 1994). Here we briefly present a time series of the sound speed measured during one of these experiments.

Figure 8 shows time series of the sound-speed anomaly for 10-kHz acoustic pulses taken simultaneously at depths of 0.5, 0.75, and 1.0 m. The sound-speed anomaly is defined as $\Delta c = c_w - c$, where c_w and c are the speed of sound in bubble-free water and in the bubbly mixture, respectively. The bubble-free sound speed c_w is obtained from measurements at sea during very calm conditions when there is no breaking. Note that the temperature is continuously recorded during the experiment in order to compensate for the variations of c_w with temperature. The data show that the signals at different depths are clearly correlated,
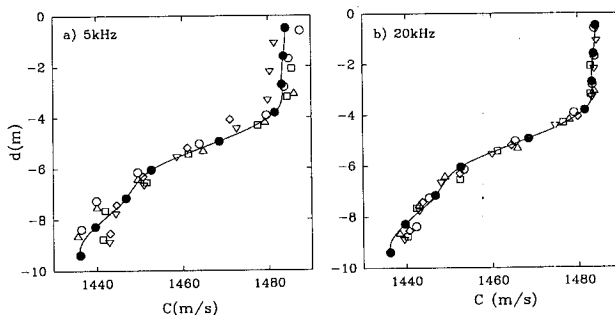

FIG. 7. (a) 5 kHz. (b) 20 kHz. Changes in sound-speed caused by variations in the temperature with depth in the Mystic Lake. Solid symbols (●) and spline fit are sound-speed measurements inferred from temperature measurements. Hollow symbols are direct sound-speed measurements from different acoustic modules.
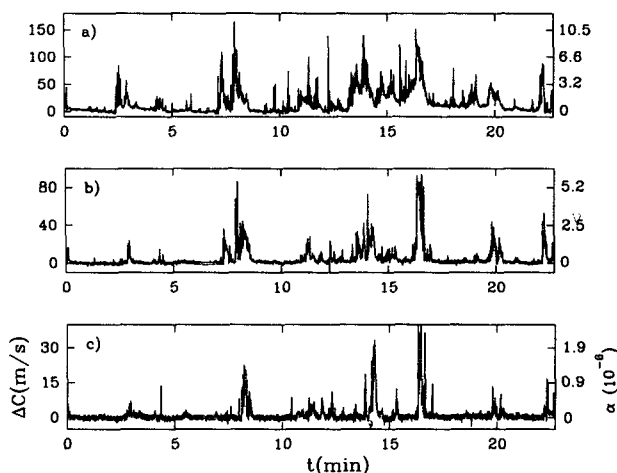
FIG. 8. Sound-speed anomalies at depths (a) 0.5 m, (b) 0.75 m, and (c) 1.0 m. Note the different vertical axes for all three plots. The axes on the right-hand side show the corresponding void fraction. The frequency of the acoustic pulses was 10 kHz. The wind speed and the SWH were 8 m s^{-1} and 0.45 m, respectively. Sampling rate was 2 Hz per channel. Data from an experiment in Buzzards Bay, Massachusetts.

FIG. 9. Sound-speed anomalies at depth 0.5 m. Two-minute section of the time series in Fig. 8a.

which would suggest that the fluctuations are caused by well-defined bubble clouds advected by the sensors. The magnitude of the anomalies is also found to rapidly decrease with depth, which is consistent with the fact that the bubble density is expected to be the highest near the surface. Because of the moderate wind conditions (8 m s^{-1}), large excursions in the signal are relatively infrequent and usually followed by periods where the signal returns back to the noise level. However, the fluctuations themselves are typically very large and they clearly dominate the long-term average at all depths. Figure 9 shows a 2-min section of the time series in Fig. 8a.

The void fraction corresponding to the measured sound-speed anomaly is shown on the vertical axis on the right-hand side of Fig. 8. The void fraction was computed using Wood's equation (appendix A). The use of Wood's equation is only justified when the sound speed is nondispersive (i.e., away from bubble resonance). Simultaneous measurements of the sound speed at several frequencies were obtained using a broadband pulse. The transmitted and received pulses were digitally bandpass filtered at several discrete frequencies, and the resulting filtered pulses were cross correlated in the usual manner to obtain simultaneous sound-speed measurements at several frequencies. Figure 10 shows the sound-speed anomaly averaged over a 20-min time series over the frequency range from 6 to 40 kHz. The data show that the sound speed is nondispersive below 20 kHz at a wind speed of approximately 8 m s^{-1}. Above 20 kHz, the average sound-speed anomaly decreases rapidly and it becomes slightly negative at 35 and 40 kHz. Details of these
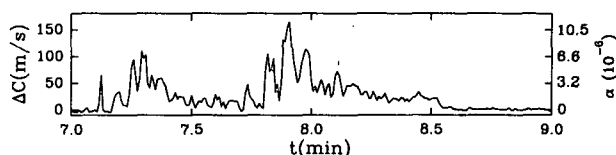
results are given elsewhere (Lamarre 1993; Lamarre and Melville 1994).

The root-mean-square (rms) noise at 10 kHz was calculated to be 0.7 m s^{-1} and the peak-to-peak noise level of the measurements is approximately ±2 m s^{-1}, which is consistent with the laboratory tests. At 5 kHz, the rms noise was found to be 2.7 m s^{-1} and the peak-to-peak noise approximately ±5 m s^{-1}. The higher noise level at 5 kHz was caused by increased ship noise at lower frequencies. For both field experiments, we have consistently observed the presence of a signal above the noise level down to a depth of 1.0 m for the highest wind conditions attained in these experiments (8 m s^{-1}). However, very few occurrences of signals above the noise level were observed at a depth of 1.5 m in the entire dataset and none at a depth of 2.0 m and greater.

7. Concluding remarks

We have reported on the development of an effective technique for measuring the low-frequency (5 kHz and above) speed of sound in the upper ocean at depths of 0.5 m and greater. Short acoustic pulses traveling over a 40-cm path from a transmit to a receive hydrophone are used to make the measurements. Phase distortions caused by acoustic reflections from the surface or from nearby structural elements are separated in time from the direct path signal by carefully balancing the pulse length, acoustic wavelength, depth of measurements, and hydrophone separation.
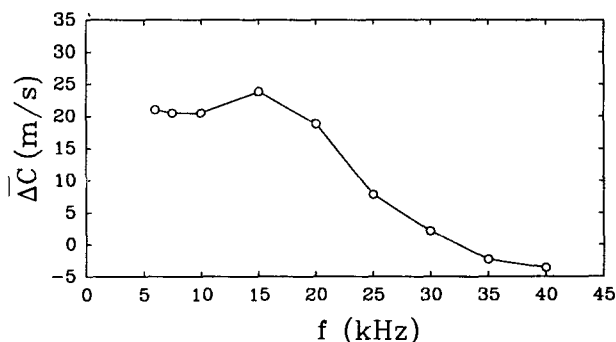

FIG. 10. Average sound-speed anomaly as a function of frequency. Averages computed over 20-min time series. Wind speed is 8 m s^{-1}. Data from an experiment in Buzzards Bay, Massachusetts.

A real-time data acquisition and data processing system was implemented to process the acoustic pulses. Prior to digitizing the data, standard analog techniques were used to condition the signal. The data were sampled at 0.5 MHz per channel and cross correlated in real time by a DSP board to extract the time delay and hence the sound speed. The maximum throughput of the system was 24 sound-speed measurements per second, including all overheads such as pulse transmission, acquisition, and data storage. In order to increase the resolution of the measurements, the cross-correlation function was interpolated in the neighborhood of its peak by a spline fit. This is only possible with signals possessing narrow bandwidths and high SNR (in the present study, SNR $\approx$ 1000 in the laboratory and SNR $\approx$ 100 in the field).

A test was performed in the laboratory by accurately varying the separation distance between the transmit and receive hydrophones. The changes in separation were measured acoustically and compared with the measurements obtain with a micrometer. The results showed that the acoustic measurements had a maximum error of $\pm 0.13\%$ over a change in separation of 25 mm and a total path length of 400 mm. For a fixed transmit–receive system, this translates into maximum errors of ± 2 m s^{-1}. Laboratory testing of the sound-speed measuring system against controlled water temperature changes have also shown that the technique can track the changes in sound speed to approximately ± 2 m s^{-1}. Similar experiments conducted in the Mystic Lake during late summer, when the temperature profile of the lake is well stratified, have shown comparable resolution for a 60 m s^{-1} spread in sound speeds. Even at frequencies as low as 5 kHz, accurate sound-speed measurements can be realized as long as the SNR is high and acoustic reflections are separated from the direct path signal.

The short segment of field data presented here has demonstrated the operation of the instrument in an ocean environment with moderate wind conditions. The time series of the sound-speed anomaly showed dramatic fluctuations over time periods on the order of minutes or less. The large fluctuations were highly correlated at various depths and they were attributed to bubble plumes or clouds that are advected and pass by the sensors. At a wind speed of 8 m s^{-1}, several occurrences of sound-speed anomalies above 100 m s^{-1} have typically been found in the 23-min time series at a depth of 0.5 m. These are the first reported time series of sound-speed anomalies in the shallow ocean surface layer (at depth comparable to the wave height) and the fluctuations measured are two to three orders of magnitude greater than previously reported time-averaged (10–20 min) measurements (Medwin 1974; Medwin et al. 1975; Farmer and Vagle 1989).

It should be pointed out that the changes in the impedance of the bubbly mixture at sea $\rho_m c_m$ are of the same magnitude as changes in the impedance of

the water in the Mystic Lake experiment. This is due to the fact that the impedance in both cases is dominated by the phase velocity c while the density ρ varies negligibly. The results from the Mystic Lake experiment show that the instrument tracked the sound-speed profile very well regardless of the change in impedance of the mixture (for sound-speed anomalies on the order of 60 m s^{-1}). Thus, we expect errors caused by changes in the impedance of the bubble mixture to be negligible for the sound-speed anomalies reported here (150 m s^{-1} or less). For much higher sound-speed anomalies (say 300 m s^{-1} or more), it is difficult to assess the effect of the change in impedance of the mixture without conducting further tests.

The laboratory and lake tests have validated the sound-speed measurement technique. The technique is capable of making simultaneous measurements of sound speed at various depths, starting as close as 0.5 m to the surface, at frequencies down to 5 kHz, and at a sample rate of 4 Hz per channel. Furthermore, the measurement technique is direct and thus avoids the many difficulties associated with inferring sound speed from incomplete bubble population data. With the present instrumentation, attenuation at various frequencies can also be obtained by measuring the amplitude of the received signal and comparing it with bubble-free measurements. With proper modifications, the system can be made autonomous and thus be deployed for long-term measurements. Such improvements are underway.

APPENDIX A

Low-Frequency Sound Speed in a Bubbly Mixture: Wood's Equation

Wood (1941) derived the speed of acoustic waves in a bubbly mixture by assuming that the mixture was homogeneous with a bulk density and compressibility. This implicitly assumes that the frequency of the pressure wave is well below the resonant frequency of the largest bubbles in the mixture and that bubbles cannot interact. The former assumption guarantees that the dispersion due to individual bubbles is negligible, and this condition is usually more exacting than the latter in typical geophysical applications (Clay and Medwin 1977). The following development is essentially that given by Wood (1941) and Karplus (1958).

Assume a mixture composed of a constituent with density ρ_a and compressibility K_a dispersed in another

constituent of density ρ_w and compressibility K_w. The proportion by volume of the first constituent is α, and by volume conservation the proportion of the second constituent is $1 - \alpha$. The sound speed of the mixture can therefore be written as

$$c_m = \frac{1}{(\rho_m K_m)^{1/2}}$$

$$= \frac{1}{\{[\alpha\rho_a + (1 - \alpha)r_w][\alpha K_a + (1 - \alpha)K_w]\}^{1/2}},$$

(A1)

where the density and the compressibility of the mixtures have been expressed as bulk quantities in accordance with the initial assumption. Experiments conducted by Karplus (1958) at frequencies much lower than the resonance frequency of the bubbles have shown that for air bubbles in water, the isothermal condition is the correct formulation for the compressibility $K_{a,\text{iso}} = 1/P$, where P is the ambient pressure. Thus, the heat exchange between the bubble and the surrounding fluid is rapid compared to one period of the pressure wave. Using the isothermal formulation for the compressibility and Eq. (A1) and noting that sound propagation in a single phase medium is adiabatic [i.e., $K_{a,\text{adi}} = 1/\gamma P$, where γ is the specific heat ratio], we obtain the following expression for the sound speed valid over the full range of void fractions

$$\frac{1}{c^2} = \frac{\alpha^2\gamma}{c_a^2} + \frac{(1 - \alpha)^2}{c_w^2} + \alpha(1 - \alpha)\left(\frac{\rho_w}{P} + \rho_a K_w\right).$$

(A2)

Figure A1 shows how the sound speed varies as a function of the void fraction in an air–water mixture. Below a 10^{-2} void fraction, the density ρ_m is relatively constant and all of the sound-speed reduction comes from the large increase in the compressibility K_m of the mixture. Above a 10^{-2} void fraction, the compressibility is relatively constant because it is dominated by the air bubbles, but the density of the mixture decreases such that the sound speed increases rapidly toward its value in air.

Verifications of Wood's equation have been performed at intermediate void fractions (10^{-4}–10^{-1}) (Silberman 1957) and high void fractions (10^{-2}–1) (Karplus 1958; Ruggles 1987) and they have confirmed its validity over those ranges. However, no experiments have been performed at low void fractions (10^{-8}–10^{-5}), mainly because of the difficulty involved in independently measuring such low void fraction and in generating a steady and controlled bubble population at small air concentrations.

APPENDIX B

Group Velocity Versus Phase Velocity

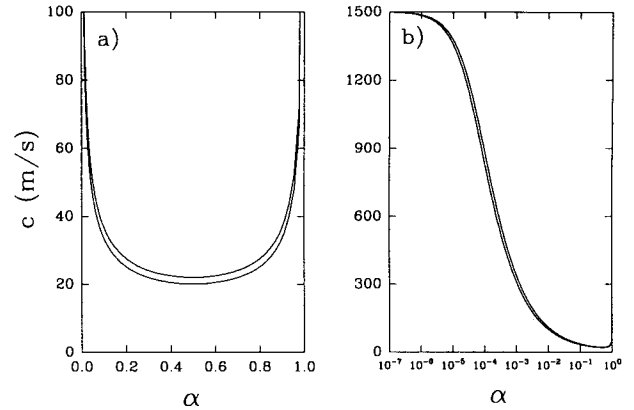In a bubbly mixture, the sound velocity at acoustic frequencies near bubble resonance is dispersive. The

FIG. A1. Low-frequency sound speed as a function of void fraction. (a) Linear–linear scale. (b) Log–linear scale. The lower curve on both plots is for atmospheric pressure and ambient temperature. The upper curve is for atmospheric pressure and a hydrostatic pressure corresponding to a depth of 2 m and ambient temperature. Typical values of the parameters used in Eq. (A2) are $c_a = 3.4 \times 10^4$ cm s^{-1}, $c_w = 1.5 \times 10^5$ cm s^{-1}, $\rho_a = 1.2 \times 10^{-3}$ g cm^{-3}, $\rho_w = 1.0$ g cm^{-3}, $P = 1.01 \times 10^6$ dyn cm^{-2} (atmosphere), $K_w = 4.54 \times 10^{-11}$ cm^2 dyn^{-1}, $\gamma = 1.4$ (Karplus 1958).

dispersion relation is entirely determined by the bubble population through which the sound must propagate [detailed presentation of the dispersion effect caused by bubbles can be found in Clay and Medwin (1977)]. Dispersion causes acoustic waves of different frequencies to propagate at different phase velocities. In the case of an acoustic pulse, we must therefore differentiate between the apparent velocity of the pulse given by its group velocity and the phase velocity of the different frequency components making up the pulse. In this appendix, we assess the effect caused by differences in group and phase velocities on our measurement of the phase velocity.

To investigate this issue, we propose a simple numerical model of the propagation of an acoustic pulse between a transmitter and a receiver. The propagation distance between the transmitter and the receiver is set at $d = 0.4$, which is consistent with the experimental setup. The transmit and received pulses are synthesized by multiplying a sine wave of frequency f by a cosine window of width $2.5c_0/f$, where c_0 is the sound speed in bubble-free water. This representation of the transmit (and received) pulse is also consistent with the experimental technique (Fig. 3). We assume that the carrier wave travels from the transmitter to the receiver at its phase velocity c_p, while the envelope of the signal (i.e., the cosine window) travels at the group velocity c_g. When the phase and the group velocity are equal (i.e., the medium is nondispersive), the transmit and received pulses are identical since both the carrier wave and its envelope travel at the same velocities. However, when the velocities are different, the received pulse will not be identical to the transmit signal. The lag or lead of the envelope on the carrier wave will depend on the

difference between the two velocities. This "sliding" of the envelope will tend to bias the location of the peak in the cross correlation of the transmitted and received signals and thus it will also bias our measurement of the phase velocity.

The phase velocity can be described by

$$c_p(f) = (c_0 - \Delta c) + bf^2, \qquad \text{(B1)}$$

where b is a constant and bf^2 is a quadratic function representing the sound-speed anomaly at a certain frequency f. This representation is in agreement with previous measurements by Medwin et al. (1974) and our own (Lamarre 1993; Lamarre and Melville 1994). The slope of the phase velocity $dc_p/df = 2bf$ becomes very small at low frequencies, consistent with the fact that the phase velocity becomes nondispersive. By definition, this functional form also yields that the maximum sound-speed reduction Δc is obtained when $f = 0$. From the measurements presented in this paper (Fig. 8), we anticipate that the frequency dependent sound-speed anomaly bf^2 is much smaller than the phase velocity c_p. The group velocity is defined as (Morse and Ingard 1968)

$$\frac{1}{c_g} = \frac{d}{df}\left(\frac{f}{c_p}\right), \qquad \text{(B2)}$$

and by substituting c_p, we obtain that

$$c_g \approx c_p + 2bf^2, \quad \text{valid for} \quad \frac{2bf^2}{c_p} \ll 1, \qquad \text{(B3)}$$

which suggests that the group velocity should differ from the phase velocity by a quantity $2bf^2$ equal to twice the sound-speed anomaly at a frequency f. We define the group velocity as $c_g = c_p(1 + \alpha)$, where $\alpha = 2bf^2/c_p$ is a parameter characterizing the difference between the phase and the group velocity. For example, $\alpha = 0.1$ would correspond in our model to a sound-speed anomaly $bf^2 = 75$ m s^{-1}, which is typical of field measurements (Fig. 8).

Figure B1 shows the results of the simulation for two different values of α. The envelope of the transmit and received pulses are shown in Figs. B1a and B1d. In order to facilitate comparisons between the transmit and the received signals, we have shifted back in time the received envelope by a period corresponding to d/c_p. Thus, if $c_g = c_p$ the two envelopes would be indistinguishable, but if $c_g > c_p$ the received envelope is to the left of the transmit envelope. The actual transmit and received pulses are obtained by multiplying the carrier wave propagating at c_p by the respective envelopes. The results are shown in Figs. B1b and B1e, where the received signals were again shifted back in time by d/c_p. The propagation velocity is obtained by cross-correlating the transmit and received pulses. In the case when $c_g = c_p$, the peak of the cross correlation should be located at $t = 0$ since the received signal was shifted back by d/c_p. For the case when $\alpha = 0.1$, the
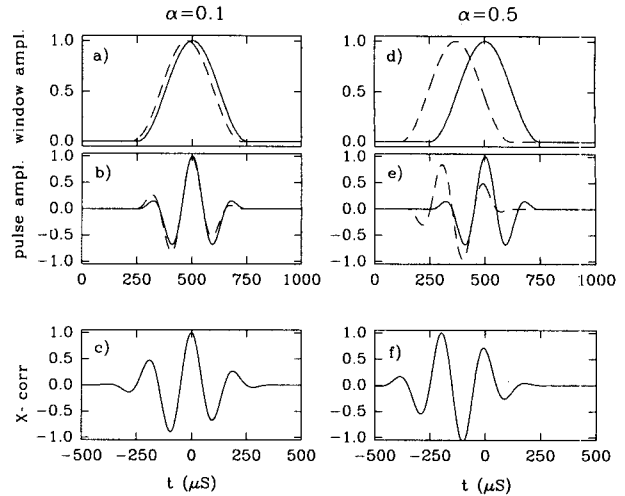

FIG. B1. Results from the numerical model for $\alpha = 0.1$ and $\alpha = 0.5$. The carrier frequency is $f = 5$ kHz. (a) and (d) Amplitude of the pulse envelopes propagating at c_g. Solid line is the transmit envelope $E_1(t)$ and dashed line is the received envelope $E_2(t - d/c_p)$ (i.e., shifted to the left by d/c_p). (b) and (e) Pulse shape obtained by multiplying the carrier wave propagating at c_p by the pulse envelope in (a) and (d). Solid line is the transmit pulse $\eta_1(t)$ and dashed line is the received pulse $\eta_2(t - d/c_p)$. (c) and (f) Cross correlation between η_1 and η_2. The location of the peak in the cross-correlation function in (c) is at -2.5 μs.

peak of the cross correlation is located at $t = -1.25$ μs, which represents the error caused by an envelope propagating at a velocity 10% faster than the phase velocity. In this particular case, the true time delay is given by $d/c_p = 0.4$ m/1425 m s^{-1} = 280.7 μs. Thus, the error on c_p caused by a c_g 10% faster is approximately 0.45% or 6 m s^{-1}. Since the signal of interest is the sound-speed anomaly, we readily obtain that the error on the measurement of the anomaly is approximately 8% (or 6 m s^{-1}/75 m s^{-1}). We conclude that measurements of the phase velocity near the ocean surface may have a bias error caused by differences between the phase and group velocity on the order of 8% (of the actual anomaly measurement). Of course, this estimate is dependent on the initial assumption concerning the functional form of $c_p(f)$, which was assumed to be quadratic [Eq. (B1)]. A functional form with an anomaly varying as bf instead of bf^2 would also be appropriate away from $f = 0$ and in this case the above development would lead to a 4% error (instead of 8%). We therefore conclude that differences in group and phase velocities will lead to small errors (4%–8%) on the measurement of the true phase velocity anomaly.

When α becomes large (i.e., $\alpha > c_p/2fd$), the envelope leads the carrier wave so much that the cross correlation abruptly jumps backward (toward smaller time delays) by a full period of the carrier wave. Such jumps in the location of the peak of the cross correlation translate in very large discontinuities in the anomaly

measurements (much larger than the typical anomalies measured). For example, in the case when $\alpha = 0.5$, the earlier arrival of the envelope leads to an error of -200 μs in the time delay (the true time delay being $d/c_p = 0.4$ m/1200 m s^{-1} = 333 μs). Thus, the propagation velocity measured is 0.4 m/(333 $-$ 200 μs) = 3007 m s^{-1} instead of the correct value of 1200 m s^{-1}. Such large and discontinuous increases in the measured phase velocity have not been observed in our dataset even for anomalies up to 800 m s^{-1}. We thus conclude that for large values of α ($\alpha > c_p/2fd$), the difference between the phase and the group velocity is probably much smaller than that suggested by the present model [Eq. (B3)].

REFERENCES

Baldy, S., 1988: Bubbles in the close vicinity of breaking waves: Statistical characteristics of the generation and dispersion mechanism. *J. Geophys. Res.,* **93,** 8239–8248.

Buckingham, M. J., 1991: On acoustic transmission in ocean-surface waveguides. *Phil. Trans. R. Soc. Lond.,* **A335,** 513–555.

Clay, C. S., and H. Medwin, 1977: *Acoustical Oceanography.* John Wiley & Sons, 544 pp.

Del Grosso, V. A., 1974: New equation for the speed of sound in natural waters (with comparisons to other equations). *J. Acoust. Soc. Am.,* **56,** 1084–1091.

Ding, L., 1992: Acoustical studies of breaking waves in the open ocean. Ph.D. thesis, University of Victoria & Institute of Ocean Science, B.C., Canada, 156 pp.

Farmer, D. M., and S. Vagle, 1989: Waveguide propagation of ambient sound in the ocean surface bubble layer. *J. Acoust. Soc. Am.,* **86,** 1897–1908.

Henyey, F. S., 1991: Acoustic scattering from microbubble plumes in the 100 Hz to 2 kHz region. *J. Acoust. Soc. Am.,* **90,** 399–405.

Karplus, H. B., 1958: The velocity of sound in a liquid containing gas bubbles. United States Atomic Energy Commission. [NTIS C00-248.]

Lamarre, E., 1993: An experimental study of air entrainment by breaking waves. Ph.D. thesis, Massachusetts Institute of Technology and Woods Hole Oceanographic Institution, MA, 327 pp.

——, and W. K. Melville, 1991: Air entrainment and dissipation in breaking waves. *Nature,* **351,** 469–472.

——, and ——, 1992: Instrumentation for the measurement of void-fraction in breaking waves: Laboratory and field results. *J. Ocean. Eng.,* **17,** 204–205.

——, and ——, 1994: Sound-speed measurements near the ocean surface. *J. Acoust. Soc. Am.,* **96,** 3605–3616.

Laville, F., G. D. Abbott, and M. J. Miller, 1991: Underwater sound generation by rainfall. *J. Acoust. Soc.,* **89,** 715–721.

Loewen, M. R., and W. K. Melville, 1991: Microwave backscatter and acoustic radiation from breaking waves. *J. Fluid Mech.,* **224,** 601–623.

Medwin, H., 1970: In situ acoustic measurements of bubble populations in coastal waters. *J. Geophys. Res.,* **75,** 599–611.

——, 1974: Acoustic fluctuations due to microbubbles in the near-surface ocean. *J. Acoust. Soc. Am.,* **75,** 1100–1104.

——, 1975: Speed of sound in water: A simple equation for realistic parameters. *J. Acoust. Soc. Am.,* **58,** 1318–1319.

——, 1977: In situ acoustic measurements of microbubbles at sea. *J. Geophys. Res.,* **82,** 971–976.

——, and N. D. Breitz, 1989: Ambient and transient bubble spectral densities in quiescent seas and under spilling breakers. *J. Geophys. Res.,* **94,** 12 751–12 759.

——, J. Fitzgerald, and G. Rautman, 1975: Acoustic miniprobing for ocean microstructure and bubbles. *J. Geophys. Res.,* **80,** 405–413.

Merlivat, L., and L. Memery, 1983: Gas exchange across an air-water interface: Experimental results and modeling of bubble contribution to transfer. *J. Geophys. Res.,* **88,** 707–724.

Morse, P. M., and K. U. Ingard, 1968: *Theoretical Acoustics.* McGraw-Hill, 927 pp.

Nystuen, J. A., 1986: Rainfall measurements using underwater ambient sound. *J. Acoust. Soc. Am.,* **79,** 972–982.

Quazi, A. H., 1981: An overview of the time delay estimate in active and passive systems for target localization. *IEEE Trans. Acoust. Speech Signal Process.,* **29,** 527–533.

Ruggles, A. E., 1987: The propagation of pressure perturbations in bubbly air/water flows. Ph.D. thesis, Mechanical Engineering, Rensselaer Polytechnic Institute, NY, 249 pp.

Silberman, E., 1957: Sound velocity and attenuation in bubbly mixtures measured in standing wave tubes. *J. Acoust. Soc. Am.,* **29,** 925–933.

Su, M.-Y., R. Burge, and J. Cartmill, 1993: Measurement of near-surface microbubble density during SWADE. *J. Geophys. Res.,* submitted.

Thorpe, S. A., 1982: On the clouds of bubbles formed by breaking waves in deep water and their role in air-sea gas transfer. *Phil. Trans. Roy. Soc. Lond.,* **A304,** 155–210.

Vagle, S., and D. M. Farmer, 1992: The measurement of bubble-size distributions by acoustical backscatter. *J. Atmos. Oceanic Technol.,* **9,** 630–644.

——, W. G. Large, and D. M. Farmer, 1990: An evaluation of the WOTAN technique of inferring oceanic winds from underwater ambient sound. *J. Atmos. Oceanic Technol.,* **7,** 576–595.

Wallace, D. W. R., and C. D. Wirick, 1992: Large air-sea gas fluxes associated with breaking waves. *Nature,* **356,** 694–696.

Wood, A. B., 1941: *A Textbook of Sound.* G. Bell & Sons, 578 pp.

Woolf, D. K., and S. A. Thorpe, 1991: Bubbles and the air-sea exchange of gases in near-saturation conditions. *J. Mar. Res.,* **49,** 435–466.

Zedel, L., and D. Farmer, 1991: Organized structures in subsurface bubble clouds: Langmuir circulation in the open ocean. *J. Geophys. Res.,* **96,** 8889–8900.